International Journal of Heat and Mass Transfer 117 (2018) 1–10

Contents lists available at ScienceDirect

International Journal of Heat and Mass Transfer

journal homepage: www.elsevier.com/locate/ijhmt

Effects of physico-chemical interfacial equilibrium on pore shape in solid

S.Y. Hsiao [a], P.S. Wei [a], L.W. Wang [b,*]

[a] Department of Mechanical and Electro-Mechanical Engineering, National Sun Yat-Sen University, Kaohsiung 80424. Taiwan, ROC
[b] School of Materials Science and Engineering, Hebei University of Science and Technology, Shijiazhuang 050018, PR China

ARTICLE INFO

Article history:
Received 16 June 2017
Received in revised form 8 September 2017
Accepted 19 September 2017
Available online 5 October 2017

Keywords:
Pore formation
Porosity
Bubble entrapment
Phase change
Porous material
Lotus-type porous material

ABSTRACT

The shape of a pore, resulting from a bubble entrapped by a solidification front, for different Henry's law constants at the cap is predicted in this work. Henry's law, indicating an interfacial physico-chemical equilibrium, is essentially required to relate solute concentration in liquid at the cap by solute gas pressure in the pore. Pore formation and its shape in solid influence contemporary issues of biology, engineering, foods, geophysics and climate change, etc. This work applies a previous model accounting for mass and momentum transport of solute across a self-consistently determined shape of the bubble cap subject to different cases characterized by different directions and magnitude of solute transport across the cap. Case 1 is referred to solute transport from the pore across cap to surrounding liquid in the early stage. Cases 2a and 2b, corresponding to low and high Henry's law constants, respectively, indicate opposite directions of species transport across the cap. An increase in Henry's law constant decreases pore radius and time for entrapment in Case 1. The pore cannot be entrapped as a pore in solid in Cases 2. The predicted pore shape in solid agrees with experimental data. Understanding, prediction and control of the growth of the pore shape have therefore been obtained.

1. Introduction

Porosity in solids is susceptible to stress concentration, degrading the mechanical properties and impeding efficiency or functional properties of products [1–8]. However, substances containing a number of pores can also be controlled and utilized as lightweight materials, catalysts, electrodes, vibration, acoustic energy absorption, impact energy absorption materials, food preservation and sterilization, and the scaffold for tissue ingrowth [8–10]. Pore formation in lotus-type porous metals containing aligned long columnar pores have been used for functionally materials in biological and medical technologies [11–13].

It has been well-known that a pore results from a single bubble entrapped by a solidification front. The bubble occurs due to supersaturated solute gas accumulated in liquid ahead of the solidification front [14] until concentration was high enough for bubbles to nucleate [15,16]. During fast growth there was less time for diffusion and the bubble decreased in cross section. When freezing was slow, bubbles were bigger. The formation of ice worms therefore was suppressed and the ice contained a large number of very small, round pores [17–19].

On the other hand, porous metals can be long cylindrical pores in ordered and aligned in one direction and fabricated by metal/gas unidirectional solidification (also called "Gasar") under a pressurized hydrogen and/or nitrogen [8,11–13]. This processing technique utilizes an invariant reaction of the so-called "metal/gas eutectic reaction" in which the melt is solidified into a solid solution and a gas phase. During solidification, the gas pore and the solid metal grow in couples and finally form a regular porous structure in which the long gas pores are aligned parallel to the solidification direction. The formed porous structure is designated as lotus-type structure because it looks like lotus roots. It was found that the lotus-type porous metals exhibit superior mechanical properties [8]. The pore diameter and interpore spacing decrease as partial pressure of hydrogen or argon increases. The porosity indicates the area ratio between the pore and its corresponding polygon. It showed that (1) the porosity decreases with the increasing of partial pressure of hydrogen when only hydrogen is used. (2) the porosity first increases and then decreases with the increasing of partial pressure of hydrogen when partial pressure of argon is kept constant, (3) the porosity decreases with the increasing of partial pressure of argon when partial pressure of hydrogen is kept constant; and (4) when the sum of hydrogen and argon pressures is constant, the porosity decreases with the increasing of partial pressure of argon [20,21].

* Corresponding author.
E-mail addresses: macplayer.tw@yahoo.com.tw (S.Y. Hsiao), pswei@mail.nsysu.edu.tw (P.S. Wei), wangliwei110127@163.com (L.W. Wang).

https://doi.org/10.1016/j.ijheatmasstransfer.2017.09.075
0017-9310/

Nomenclature

A_c	cap surface area $A_c = \tilde{A}_c/\tilde{R}_0^2 \approx 2\pi R^2(0)(1-\cos\phi_B)$
Bo	Bond number, $Bo \equiv \rho g \tilde{R}_0^2/\sigma$
C_∞	initial solute concentration,$C_\infty = \tilde{C}_\infty \tilde{R}_u \tilde{T}/\rho g \tilde{R}_0$
D	solute diffusivity
h_B	liquid depth, as illustrated in Fig. 1(a)
h_D	mass transfer coefficient, $h_D = \tilde{h}_D \tilde{R}_0/\tilde{D}$
K	Henry's law constant, $K = \tilde{K}/\tilde{R}_u\tilde{T}$
L	micro-bubble radius at $\pi/2$
p	pressure, $p \equiv \tilde{p}\tilde{R}_0/\sigma$
r	cylindrical coordinate, $r \equiv \tilde{r}/\tilde{R}_0$
R	radius, $R \equiv \tilde{R}/\tilde{R}_0$
R(0)	radius of curvature at micro-bubble apex
R_u	universal gas constant
s	solidification front location
t	time, $t = \tilde{t}\tilde{D}/\tilde{R}_0^2$
U	solidification rate, U = ds/dt
V	volume, $V = \tilde{V}/\tilde{R}_0^3$
z	cylindrical coordinate, $z \equiv \tilde{z}/\tilde{R}_0$

Greek letter

σ	surface tension
ρ	density
ϕ	inclination angle

Subscripts

a	atmosphere
c	cap
B	base
g	gas
0	initial state

Superscripts

$\sim$	dimensional quantity

Solute gas transport across the bubble cap and the free surface of the liquid require application of the Henry's law or Sievert's law governing physico-chemical equilibrium [11–13,15,20–23]. In view of different solubilities of liquid and gas, solute concentration across the bubble cap and free surface of liquid is segregated. Similar to equilibrium partition coefficient required for solute segregation between liquid and solid during solidification, Henry's law is needed to describe a relationship between gas pressure and solute gas concentration in equilibrium at a gas-liquid interface or the bubble cap. An introduction of Henry's constant can avoid complicated determination of solute concentration at the bubble cap, provided that gas pressure in the pore is found. Likewise, an introduction of equilibrium partition coefficient can avoid determination of solute concentration in solid if solute concentration in liquid at the solidification front is known.

A steady-state solute concentration field ahead of the hemispherical portion of a single cylindrical gas bubble entrapped in a growing crystal was numerically solved by Zhdanov et al. [24]. Since physico-chemical equilibrium at the bubble cap was not accounted for, time-dependent solute concentration and solute gas pressure in the pore were not presented. Time-dependent solute gas pressure is essentially required to determine growth of the bubble cap, resulting in the development of the pore shape in solid. It showed that solute concentration increased near the solidification front whereas decreased near the axisymmetric axis. Considering physico-chemical equilibrium at the free surface away from the solidification front, Liu et al. [12] provided analytical solute transport in terms of summation of different orders of Bessel's function in the gasar eutectic growth in a directional solidification subject to a flat top bubble. A more complete steady state solution of concentration field around a self-consistent shape of the bubble cap in gasar eutectic growth in a directional solidification subject to physico-chemical equilibrium at the free surface away from the solidification front was also provided by Li et al. [25] using multiple scale expansion and matching method for a small Peclet number.

Solute gas dissolved in the liquid is satisfied by a physico-chemical equilibrium governed by Sievert's law or Henry law at the free surface. On the other hand, solute gas is rejected into the liquid as the solid–liquid interface is advanced. When solidification occurs at the intersection of the solid–melt interface and the rim of the bubble cap, the solid again first rejects gas solute to the liquid side at the bubble surface. Since the melt there is slightly oversaturated with solute, for the pressure that is fixed by the environment, the gas is quickly released from the melt into the bubble in compliance with Henry's law. Therefore, the melt upon solidification at the bubble surface effectively releases the gas solute into the bubble instead of to the melt side, thus alleviating solute build-up. Enhanced mass transport to the cap from surrounding liquid and gas pressure in the bubble led to a decrease of cap radius in order to satisfy balances of pressures at the cap [22,23].

In this work, the shape of a pore resulting from a bubble entrapped by a solidification front for different Henry's law constants is predicted. The pore shape is dominated by solute transport due to difference in solute concentrations far from the solidification front and at the bubble cap [26]. The effects of Henry's law coefficient responsible for solute concentration at the bubble cap and solute gas pressure in the pore on the pore shape are therefore important. A realistic pore shape in solid, transient deformation of the bubble cap above the solidification front and solute gas concentration due to nucleation are included. Rigorous understanding of the effects of physico-chemical equilibrium on the growth of the pore shape are obtained.

2. System model and analysis

A pore in solid resulting from an entrapped bubble by a solidification front is illustrated in Fig. 1(a). A realistic shape of the bubble cap is determined by the Young-Laplace equation governing pressure balance between gas, capillary and liquid pressures. Solute gas pressure in the pore is determined by solute transport across the cap in different directions, as illustrated in Fig. 1 (b) and (c). The former, Case 1, is referred to solutes transport from the pore across an emerged cap through a concentration boundary layer on the solidification front into surrounding liquid in the early stage, whereas the latter, Case 2, is applicable to solute transport from the concentration boundary layer across a submerged cap into the pore. The major assumptions made are the following:

1. The model system is axisymmetric.
2. The tiny bubble is defined by a small Bond number, leading to application of available perturbation solutions to predict a lumped bubble in a spherical cap-shape [27]. Bond number is usually much smaller than unity for a typical bubble radius smaller than 10^{-4} m.

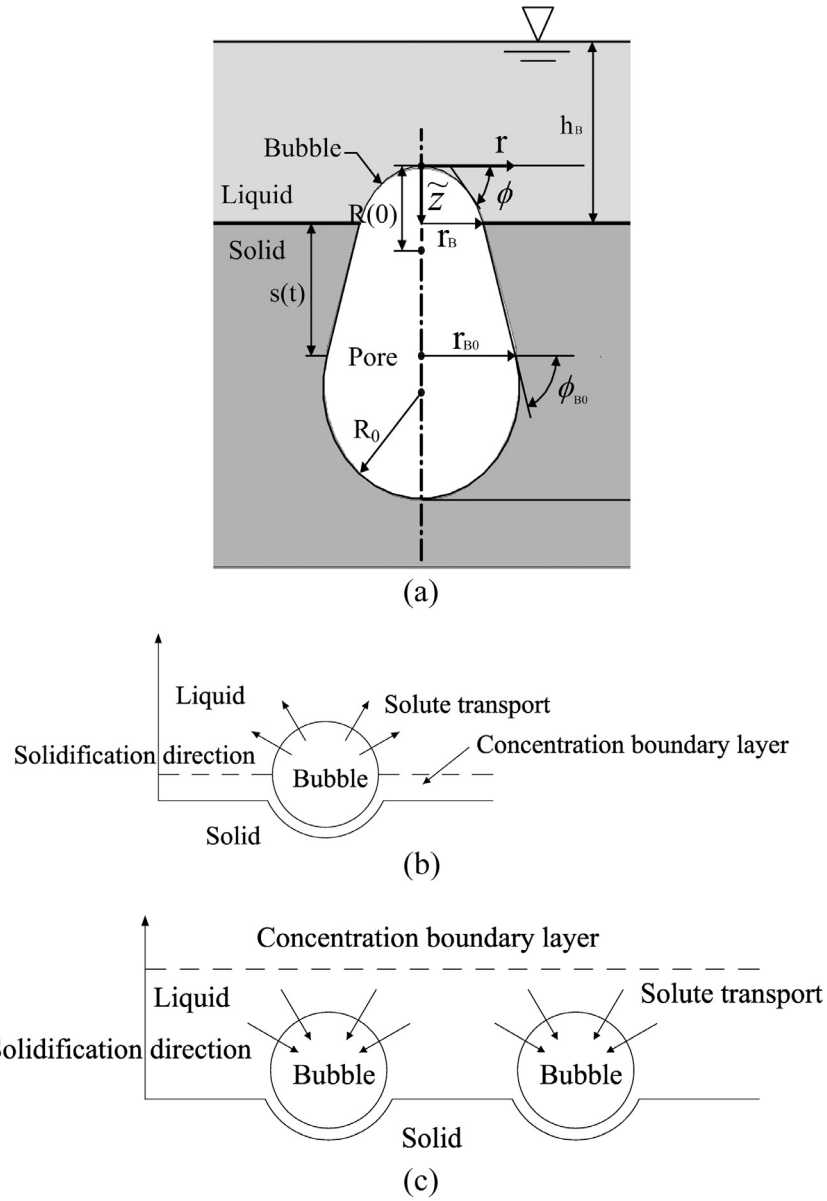

Fig. 1. Schematic of (a) physical model, (b) outward solute transport across an emerged cap through a concentration boundary layer in Case 1, and (c) inward solute transport across a submerged cap in a concentration boundary layer in Case 2.

3. The system is static. Tangential and normal viscous stresses in the liquid are therefore neglected. Liquid pressure is hydrostatic pressure.
4. Solute transfer across the bubble cap, leading to an increase in number of moles of solute gas per unit time in the pore, is given by [28].

$$\frac{d\tilde{n}_g}{d\tilde{t}} = \tilde{h}_D \tilde{A}_c (\tilde{C}_\infty - \tilde{C}_c) \tag{1}$$

where $\tilde{n}_g$, $\tilde{h}_D$, $\tilde{A}_c$, $\tilde{C}_\infty$ and $\tilde{C}_c$ are, respectively, dimensional solute content in the pore, mass transfer coefficient, surface area of the cap, and solute concentrations in liquid far from the solidification front and on the bubble cap. Since the bubble is nucleated due to supersaturation, Eq. (1) indicates that solute transport is from the pore to surrounding liquid in the early stage. On the other hand, solute transport to the bubble cap can also be given by [22,23,29,30]

$$\frac{d\tilde{n}_g}{d\tilde{t}} = \tilde{h}_D \tilde{A}_c (\tilde{C}_c - \tilde{C}_\infty) \tag{2}$$

where the term on the right-hand can be considered as a solute source. This is attributed to solute accumulation ahead of the advancing interface between solid and liquid. Cox et al. [29] and Lee et al. [30] showed that concentration gradient between the solidification front and bubble cap results in solute transport from the side along the solidification front to the pore.

5. Physico-chemical equilibrium governed by Henry's law at the bubble cap is

$$\tilde{C}_c = \frac{\tilde{p}_g}{\tilde{K}} \tag{3}$$

where $\tilde{p}_g$ and $\tilde{K}$ are, respectively, dimensional solute gas pressure in the pore and Henry's law coefficient. Eq. (3) indicates solute gas pressure is proportional to solute concentration in the liquid at a liquid-gas interface.

6. Pore shape is delineated by tracing contact angle of the bubble cap beyond the solidification front.
7. Solidification rate is specified. Otherwise, solving unsteady energy equation together with Stefan condition at the solidification front is needed.

The governing equation of gas pressure in the pore can be obtained by taking time derivative of the equation of state

$$\frac{d\tilde{p}_g}{d\tilde{t}}\tilde{V}+\tilde{p}_g\frac{d\tilde{V}}{d\tilde{t}}=\frac{d\tilde{n}_g}{d\tilde{t}}\tilde{R}_u\,\tilde{T} \tag{4}$$

where $\tilde{V}$ and $\tilde{R}_u$ are, respectively, total volume of pore and bubble cap below and above the solidification front, and universal gas constant. Substituting Eqs. (1) and (3) into Eq. (4) leads to a dimensionless equation

$$\frac{dp_g}{dt}+\frac{p_gA_c}{V}\left(\frac{1}{A_c}\frac{dV}{dt}+\frac{h_D}{K}\right)=\frac{h_DBoA_c}{V}C_\infty \tag{5}$$

where Bond number $Bo\equiv\rho g\tilde{R}_0^2/\sigma$, defined as the ratio between hydrostatic pressure and capillary pressure in a length scale of initial bubble radius. Similarly, substituting Eqs. (2) and (3) into Eq. (4) gives

$$\frac{dp_g}{dt}+\frac{p_gA_c}{V}\left(\frac{1}{A_c}\frac{dV}{dt}-\frac{h_D}{K}\right)=-\frac{h_DBoA_c}{V}C_\infty \tag{6}$$

where analytical solutions of Eqs. (5) and (6) can be readily obtained. Examining Eqs. (5) and (6) indicates that there exist three cases

$$\frac{1}{A_c}\frac{dV}{dt}+\frac{h_D}{K}>0\quad\text{for Case 1} \tag{7}$$

$$\frac{1}{A_c}\frac{dV}{dt}-\frac{h_D}{K}<0\quad\text{for Case 2a} \tag{8}$$

$$\frac{1}{A_c}\frac{dV}{dt}-\frac{h_D}{K}>0\quad\text{for Case 2b} \tag{9}$$

which indicates dimensionless Henry's law constant plays an important role in solute gas pressure in the pore. The first term on the left-hand side of Eqs. (7)–(9) is related to solidification rate, which is revealed by the ratio between expansion rate of pore volume and surface area of the cap, whereas the second term is referred to solute transport across the cap. Pore volume composed of volumes below and above the solidification front in Eqs. (5) or (6) is determined as the bubble shape is found. The cap shape in absence of an inflection point and neck region is found to be [27,31]

$$r=L\left(\sin\phi-\frac{\pi-\phi}{2}+\frac{1}{2}\sqrt{(\pi-\phi)^2-\frac{8}{3}L^2Bo}\right)+\frac{1}{3}L^3Bo\left(\frac{2}{\pi-\phi}-\cos^2\phi\tan\frac{\phi}{2}\right) \tag{10}$$

$$z=L\left[1-\cos\phi+\left(\frac{\pi-\phi}{2}\right)^2-\frac{\pi-\phi}{4}\sqrt{(\pi-\phi)^2-\frac{8}{3}L^2Bo}\right]-\frac{2}{3}L^3Bo\left\{\frac{1}{2}\left(1+\cos\phi-\cos^2\phi+2\ln\cos\frac{\phi}{2}\right)+\ln\left(\frac{1}{2(\pi-\phi)}\sqrt{(\pi-\phi)^2-\frac{8}{3}L^2Bo}+\frac{1}{2}\right)\right\} \tag{11}$$

where ϕ is contact angle of the bubble cap. Bubble radius at inclination angle of 90 degrees yields

$$L=R(0)+\frac{1}{6}R(0)^3Bo+O(Bo^2) \tag{12}$$

where R(0) is apex radius of the bubble cap. Apex radius of the cap can be determined by the Young-Laplace equation

$$p_g=Bo(h_B-z_B)+p_a+\frac{2}{R(0)} \tag{13}$$

where h_B and z_B are, respectively, thickness of liquid layer and height of the bubble cap. Eq. (13) at the initial time yields

$$p_{g0}=Bo(h_{B0}-z_{B0})+p_a+2 \tag{14}$$

Subtracting Eq. (14) by Eq. (13) gives peak radius of the bubble cap

$$R(0)=\frac{2}{2+p_g-p_{g0}+Bo(h_{B0}-h_B-z_{B0}+z_B)} \tag{15}$$

which is automatically satisfied by R(0) = 1 at the initial time t = 0. The height $z_{B0}=1-\cos\phi_{B0}$, is the initial height of the bubble cap. Apex radius of the bubble cap increases as solute gas pressure in the pore and hydrostatic pressure in surrounding liquid decrease. Solute gas pressure in the pore is dominated by Henry's law constant. Continuity of the slope between the bubble cap and pore in the solid at the level of the solidification front is needed (see Fig. 1(a)) [23]

$$\frac{dr_B}{ds}=\frac{1}{\tan(\pi-\phi_B)} \tag{16}$$

where r_B and s are, respectively, base radius of the bubble cap and location of the solidification front. Eq. (16) indicates that pore shape is delineated from tracing contact angle of the cap.

2.1. Solution procedure

The solution procedure is as follows:

1. Select initial conditions R(0) = 1, ϕ_{B0}, h_{B0}, and solidification rate U, and independent dimensionless parameters K, C_∞, Bo, and h_D.
2. Calculate cap base radius r_B from Eq. (16), and L from Eq. (12).
3. Determine contact angle ϕ_B from Eq. (10).
4. Calculate cap height z_B from Eq. (11).
5. Calculate pore volume V.
6. Calculate gas pressure p_g from Eq. (5) or (6).
7. Calculate cap radius R(0) from Eq. (15).
8. Go to step 2 for the next time.

3. Results and discussion

In this work, independent dimensionless parameters were estimated from a bubble in typical sizes of $10^{-4}-10^{-6}$ m nucleated on a solidification front with a solidification rate $10^{-5}-10^{-6}$ m/s in cooling water containing dissolved carbon dioxide gas around 0.001–0.3 wt%. Solute diffusivity in liquid was chosen to be $10^{-7}-10^{-9}$m^2/s, mass transfer coefficient was 10^{-6}m/s, Henry's law constant was 10^6-10^8 Pa/wt%.

The pore shape has a singularity at contact angle of 90 degrees [23]. A narrow range between 90.01 and 89.99 degrees is thus excluded to reach convergence, as can be seen in Fig. 2. The measured and predicted contact angle and pore radius agree with experimental data [32], as shown in Fig. 3(a) and (b), respectively. There exists a long period of time at the contact angle around 90 degrees. The maximum cap radius at the solidification front corresponds to the contact angle at 90 degrees. Two cases are described as follows:

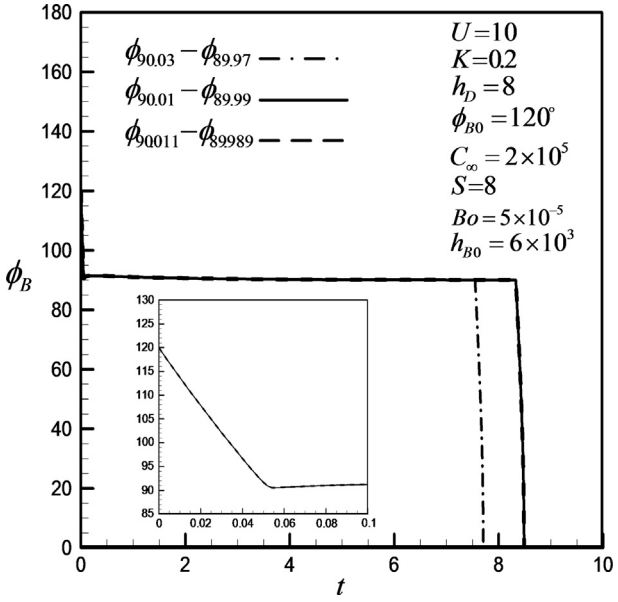

Fig. 2. Convergence test for a contact angle around 90 degrees.

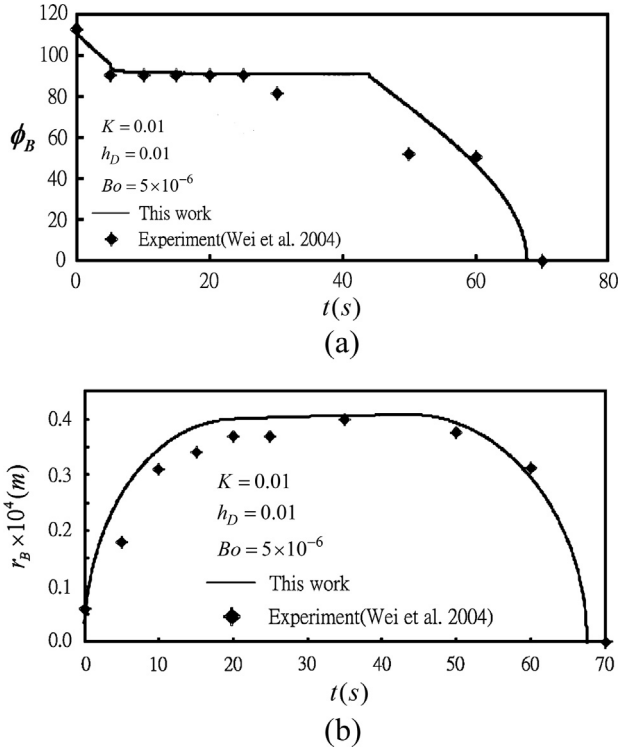

Fig. 3. Comparison between measured and predicted (a) contact angle and (b) pore radius as functions of time.

3.1. Case 1: Solute transport is from the pore to surrounding liquid in the early stage

In Case 1, predicted development of a pore from entrainment of a bubble for different dimensionless Henry's law constants is shown in Fig. 4(a). An increase in dimensionless Henry's law constant reduces pore radius and time for bubble entrapment. Provided that typical solute diffusivity in liquid is 10^{-9} m^2/s and initial bubble radius is 10^{-5} m, scales of time and pore radius for bubble entrapment, are, respectively, 100 s and 10^{-5} m for a dimensionless time of 10. These values are consistent to experimental data shown in Fig. 3(b). Fig. 4(b) shows that solute concentration at the cap decreases rapidly in the early stage. Solute concentration further becomes lower than initial concentration in liquid, leading to change in directions of solute transport from surrounding liquid to the pore in the late stage. The trend of solute concentration at the cap in the early and late stages are, respectively, attributed to additive and competitive effects of pore volume expansion with solute transport from the pore to surrounding liquid and vice versa. An increase in dimensionless Henry's law constant decreases solute concentration at the cap. This is attributed to a decrease in initial solute concentration at the cap, as can be seen from Eq. (3). The difference between solute concentration at the cap and that far from the solidification front indicates that an increase in dimensionless Henry constant decreases and increases solute transport across the cap in the early and late stages, respectively.

The corresponding product of dimensionless solute gas pressure and volume as a function of time confirms magnitude and direction of solute transfer between the bubble cap and liquid, as shown in Fig. 4(c). Based on Eqs. (1) and (4), a negative time derivative of product of dimensionless solute gas pressure and volume in the pore implies solute is transferred from the pore across cap to surrounding liquid in the early stage, because bubble is initiated by nucleation due to supersaturation. As solute transport is from the surrounding liquid to pore, the product of gas pressure and pore volume increases in the late stage. Time derivative of product of solute gas pressure and volume of the pore with time reveals that an increase in dimensionless Henry's law constant decreases and increases solute transport across the cap in the early and late stage, respectively. To satisfy physico-chemical equilibrium, the trend of solute gas pressure in the pore during solidification is similar to solute concentration at the cap, as shown in Fig. 4(d). An increase in dimensionless Henry's law constant increases dimensionless solute gas pressure in the pore, as can be seen from Eq. (3). In order to satisfy pressure balance at the bubble cap, apex radius of the cap decreases as dimensionless Henry's law constant increases and monotonically increases in the course of solidification.

Contact angle decreases during solidification for different dimensionless Henry's law constants, as shown in Fig. 4(e). The decrease in contact angle is more rapid as dimensionless Henry's law constant increases. Contact angle then maintain a relative constant value near 90 degrees for a long period. In view of graduate decrease in increasing rate of apex radius of the cap, the bubble growth rate-to-solidification rate ratio is positive. The positive bubble growth rate-to-solidification rate ratio increases rapidly in the early state, and then gradually decreases in the late stage. As the bubble growth rate-to-solidification rate ratio becomes zero, contact angle passes through 90 degrees, leading to entrapment of the bubble. The bubble growth rate-to-solidification rate rapidly decreases to zero as dimensionless Henry's law constant increases.

3.2. Cases 2: Solute transport is from surrounding liquid into pore in the early stage

In Case 2a, an increase in dimensionless Henry's law constant increases pore radius, as shown in Fig. 5(a). Fig. 5(b) shows that solute concentration at the cap increases with time. This is attributed to the stronger effect of solute transport from the surrounding liquid across cap into pore than expansion of pore volume, as can be seen from Eq. (8). An increase in dimensionless Henry's law constant decreases solute concentration at the cap. A positive time derivative of product of dimensionless solute gas pressure and vol-

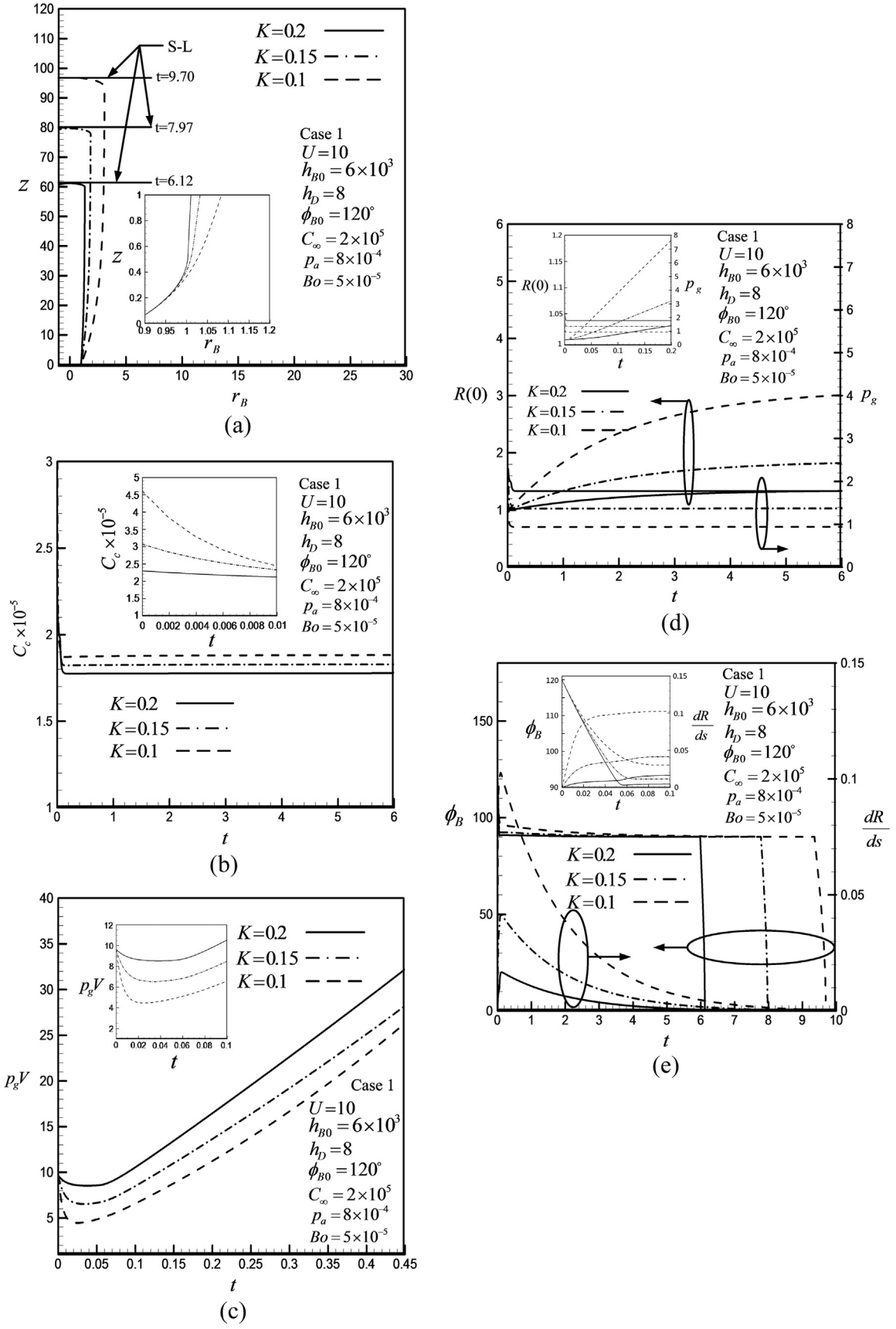

Fig. 4. Predicted (a) pore shape, and (b) dimensionless solute concentration at the cap, (c) product of dimensionless solute gas pressure and volume, (d) dimensionless apex radius and solute gas pressure, and (e) contact angle and bubble growth rate-to-solidification rate ratio as functions of time for different dimensionless Henry's law constants in Case 1.

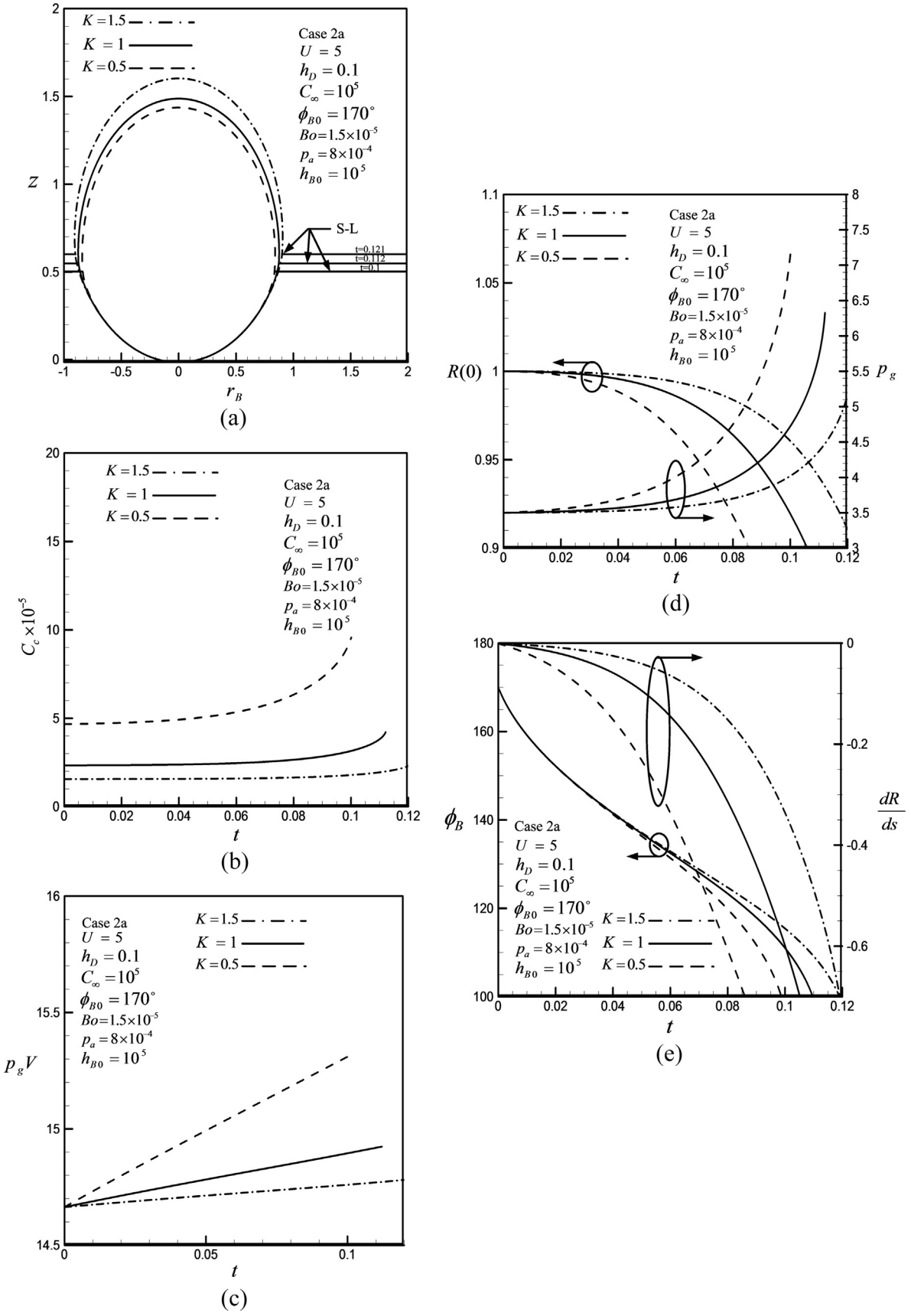

Fig. 5. Predicted (a) pore shape, and (b) dimensionless solute concentration at the cap, (c) product of dimensionless solute gas pressure and volume, (d) dimensionless apex radius and solute gas pressure, and (e) contact angle and bubble growth rate-to-solidification rate ratio as functions of time for different dimensionless Henry's law constants in Case 2a.

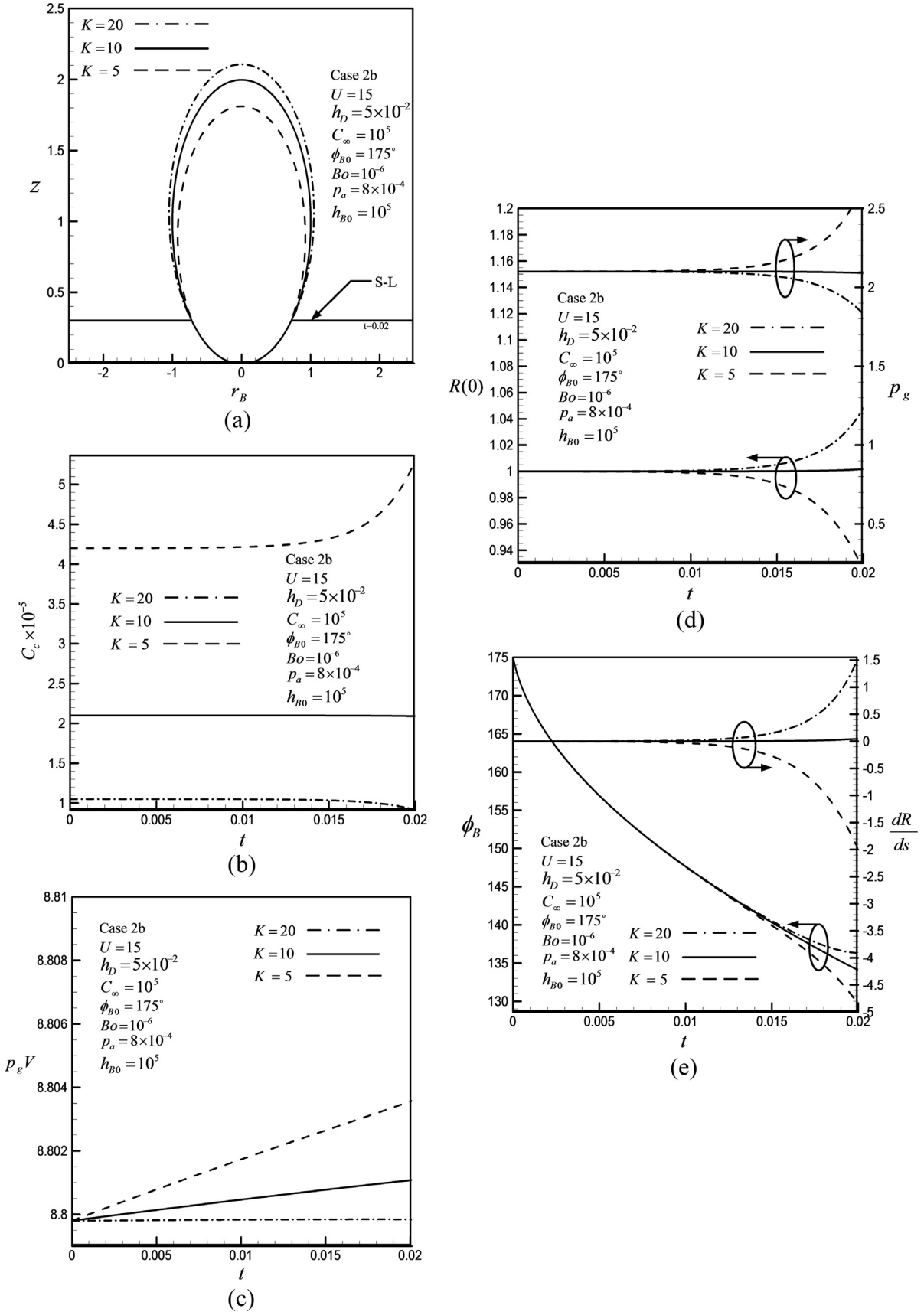

Fig. 6. Predicted (a) pore shape, and (b) dimensionless solute concentration at the cap, (c) product of dimensionless solute gas pressure and volume, (d) dimensionless apex radius and solute gas pressure, and (e) contact angle and bubble growth rate-to-solidification rate ratio as functions of time for different dimensionless Henry's law constants in Case 2b.

ume of the pore, indicating that solute transport from the surrounding liquid into pore, decreases as dimensionless Henry's law constant increases, as shown in Fig. 5(c). The corresponding apex radius of the cap decrease significantly in the late stage due to a significant increase in solute gas pressure in the pore, as shown in Fig. 5(d). An increase in Henry's law constant reduces decreasing rate of apex radius and increasing rate of solute gas pressure in the course of solidification. Fig. 5(e) shows that decreasing rates of contact angle and negative bubble growth rate-to-solidification rate ratio for an initial contact angle greater than 90 degrees decrease as dimensionless Henry's law constant increases. Since the negative bubble growth rate-to-solidification rate ratio cannot approach zero, the bubble cannot be entrapped as an isolated pore in solid.

In Case 2b, an increase in dimensionless Henry's law constant also increases pore radius, as shown in Fig. 6(a). Except for a sufficiently low dimensionless Henry's law constant of 5, solute concentration at the cap decreases during solidification, as shown in Fig. 6(b). This is attributed to the stronger effect of volume expansion of the pore than solute transport from the surrounding liquid into pore, as can be seen from Eq. (9). An increase in dimensionless Henry's law constant decreases solute concentration at the cap. A positive time derivative of product of dimensionless solute gas pressure and volume of the pore, indicating that solute transport from the surrounding liquid into pore, decreases as dimensionless Henry's law constant increases, as shown in Fig. 6(c). The corresponding apex radius of the cap increases and solute gas pressure in the pore decreases significantly in the late stage, as shown in Fig. 6(d). Apex radius increases rapidly and solute gas pressure decreases significantly in the late stage as dimensionless Henry's law constant increases. Fig. 6(e) shows that an increase in dimensionless Henry's law constant reduces decreasing rate of contact angle and enhances increasing rate of the positive bubble growth rate-to-solidification rate ratio for an initial contact angle greater than 90 degrees. Since the bubble growth rate-to-solidification rate ratio cannot approach zero, the bubble cannot be entrapped as an isolated pore in solid.

4. Conclusions

Conclusions drawn are the following:

Case 1: Solute transport is from the pore across cap to surrounding liquid in the early stage.

1. An increase in dimensionless Henry's law constant decreases pore radius and time for bubble entrapment.
2. Solute concentration at the cap decreases rapidly in the early stage, and maintain relatively constant in late stages. They are, respectively, attributed to additive and competitive effects of pore volume expansion with solute transport from the pore to surrounding liquid and vice versa. An increase in dimensionless Henry constant decreases solute concentration at the cap due to a decrease in initial solute concentration at the cap. Solute transport across the cap therefore decreases and increases in the early and late stage, respectively.
3. The trend of solute gas pressure in the pore is similar to solute concentration at the cap for a given Henry's law constant. An increase in dimensionless Henry's law constant increases dimensionless solute gas pressure in the pore and decreases apex radius of the cap. Apex radius monotonically increases with time.
4. An increase in dimensionless Henry's law constant increases decreasing rate of contact angle and decreases period for maintaining 90 degrees. The positive bubble growth rate-to-solidification rate ratio gradually decreases in the late stage. As the bubble growth rate-to-solidification rate ratio becomes zero, contact angle passes through 90 degrees, leading to entrapment of the bubble. The bubble cap is entrapped earlier as Henry's law constant increases.

Case 2: Accumulated solute ahead of the solidification front is transport from the surrounding liquid across cap into pore in the early stage. Pore radius increases with dimensionless Henry's law constant. An isolated pore is unable to form, because bubble growth rate-to-solidification rate ratio cannot approach zero. In contrast to Case 2b, the effects of solute transport on solute gas pressure in the pore in Case 2a are more significant than pore volume expansion in the late stage. An increase in Henry's law constant in Case 2a reduces increasing rates of solute gas pressure in the pore and solute concentration at the cap and decreasing rates of apex radius during solidification. In Case 2b, an increase in Henry's law constant increases deceasing rates of solute concentration at the cap and solute gas pressure in the pore and increasing rates of apex radius in the late stage.

Acknowledgment

This work is supported by NSC 102-2221-E-110-038, ROC.

References

[1] S. Kou, Welding Metallurgy, Wiley, New York, 1987.
[2] C.D. Sulfredge, L.C. Chow, K.A. Tagavi, Artificial dispersal of void patterns in unidirectional freezing, Exp. Heat Transfer 6 (1993) 389–409.
[3] J.E. Ramirez, B. Han, S. Liu, Effect of welding variables and solidification substructure on weld metal porosity, Metall. Mater. Trans. A 25 (1994) 2285–2294.
[4] H. Zhao, D.R. White, T. DebRoy, Current issues and problems in laser welding of automotive aluminum alloys, Int. Mater. Rev. 44 (1999) 238–266.
[5] J.W. Elmer, J. Vaja, H.D. Carlton, R. Pong, The effect of Ar and N2 shielding gas on laser weld porosity in steel, stainless steels, and nickel, Weld. J 94 (2015) 313-s–325-s.
[6] P.B. Oliete, J.I. Peña, Study of the gas inclusions in Al2O3/Y3Al5O12 and Al2O3/Y3Al5O12/ZrO2 eutectic fibers grown by laser floating zone, J. Crystal Growth 304 (2007) 514–519.
[7] M. Torkar, F. Tehovnik, B. Arh, M. Jenko, B. Sarler, Z. Rajic, Microstructure characteristics of the model spring steel 51CrV4, Mater. Technol. 48 (2014) 537–543.
[8] H. Nakajima, Fabrication, properties and application of porous metals with directional pores, Prog. Mater. Sci. 52 (2007) 1091–1173.
[9] M. Tane, H. Nakajima, Influence of ultrasonic agitation on pore formation and growth during unidirectional solidification of water-carbon dioxide solution, Mater. Trans. 47 (2006) 2183–2187.
[10] T. Inada, T. Hatakeyama, F. Takemura, Gas-storage ice grown form water containing mircobubbles, Int. J. Refrig. 32 (2009) 462–471.
[11] J.S. Park, S.K. Hyun, S. Suzuki, H. Nakajima, Effect of transference velocity and hydrogen pressure on porosity and poremorphology of lotus-type porous copper fabricated by a continuous casting technique, Acta Mater. 55 (2007) 5646–5654.
[12] Y. Liu, Y.X. Li, J. Wan, H.W. Zhang, Evaluation of porosity in lotus-type porous magnesium fabricated by metal/gas eutectic unidirectional solidification, Mater. Sci. Eng. A. 402 (2005) 47–54.
[13] K. Yoshimura, T. Inada, S. Koyama, Growth of spherical and cylindrical oxygen bubbles at an ice-water interface, Cryst. Growth Des. 8 (2008) 2108–2115.
[14] A.I. Fedorchenko, A.A. Chernov, Exact solution of the problem of gas segregation in the process of crystallization, Int. J. Heat Mass Transfer 46 (2003) 915–919.
[15] P.S. Wei, C.C. Huang, K.W. Lee, Nucleation of bubbles on a solidification front-experiment and analysis, Metall. Mater. Trans. B 34 (2003) 321–332.
[16] G.G. Poon, B. Peters, A stochastic model for nucleation in the boundary layer during solvent freeze-concentration, Cryst. Growth Des. 13 (2013) 4642–4647.
[17] B. Chalmers, How water freezes, Sci. Am. 200 (1959) 114–122.
[18] S.A. Bari, J. Hallett, Nucleation and growth of bubbles at an ice-water interface, J. Glaciol. 13 (1974) 489–520.
[19] K. Murakami, H. Nakajima, Formation of pores during unidirectional solidification of water containing carbon dioxide, Mater. Trans. 43 (2002) 2582–2588.
[20] S. Yamamura, H. Shiota, K. Murakami, H. Nakajima, Evaluation of porosity in porous copper fabricated by unidirectional solidification under pressurized hydrogen, Mater. Sci. Eng. A 318 (2001) 137–143.
[21] Y. Liu, Y. Li, J. Wan, H. Zhang, Metal/gas eutectic growth during unidirectional solidification, Metall. Mater. Trans. A 37 (2006) 2871–2878.

[22] P.S. Wei, Y.K. Kuo, S.H. Chiu, C.Y. Ho, Shape of a pore trapped in solid during solidification, Int. J. Heat Mass Transfer 43 (2000) 263–280.
[23] P.S. Wei, C.Y. Ho, An analytical self-consistent determination of a bubble with a deformed cap trapped in solid during solidification, Metall. Mater. Trans. B 33 (2002) 91–100.
[24] A.V. Zhdanov, G.A. Satunkin, V.A. Tatarchenko, N.N. Talyanskaya, Cylindrical pores in a growing crystal, J. Crystal Growth 49 (1980) 659–664.
[25] X.-M. Li, W.-Q. Li, Q.-L. Jin, R. Zhou, A steady solution of the gasar eutectic growth in directional solidification, Chin. Phys. B 22 (2013) 078101.
[26] P.S. Wei, S.Y. Hsiao, Effects of solute concentration in liquid on pore shape in solid, Int. J. Heat Mass Transfer 103 (2016) 920–930.
[27] S.B.G. O'Brien, On the shape of small sessile and pendant drops by singular perturbation techniques, J. Fluid Mech. 233 (1991) 519–537.
[28] S.F. Jones, G.M. Evans, K.P. Galvin, The cycle of bubble production from a gas cavity in a supersaturated solution, Adv. Coll. Interface. Sci. 80 (1999) 51–84.
[29] M.C. Cox, A.V. Anilkumar, R.N. Grugel, C.P. Lee, Effect of step-wise change in processing pressure on isolated pore growth during controlled directional solidification in small channels, J. Crystal Growth 311 (2009) 327–336.
[30] C.P. Lee, A.V. Anilkumar, M.C. Cox, C.B. Lioi, R.N. Grugel, Evolution of elongated pores at the melt-solid interface during controlled directional solidification, Acta Mater. 61 (2013) 3752–3757.
[31] P.S. Wei, C.C. Hsiao, Microbubble or pendant drop control described by a general phase diagram, Int. J. Heat Mass Transfer 52 (2009) 1304–1312.
[32] P.S. Wei, C.C. Huang, Z.P. Wang, K.Y. Chen, C.H. Lin, Growths of bubble/pore sizes in solid during solidification -an in situ measurement and analysis, J. Crystal Growth 270 (2004) 662–673.